Monthly Notices of the ROYAL ASTRONOMICAL SOCIETY

MNRAS **515,** 2208–2214 (2022) https://doi.org/10.1093/mnras/stac1873
Advance Access publication 2022 July 8

A truncated inner disc in the Seyfert 1 galaxy WKK 4438

L. C. Gallo,[1]★ M. Z. Buhariwalla,[1] J. Jiang,[2] F. D'Ammando [3] and D. J. Walton [2,4]

[1]*Department of Astronomy and Physics, Saint Mary's University, 923 Robie Street, Halifax, NS B3H 3C3, Canada*
[2]*Institute of Astronomy, University of Cambridge, Madingley Road, Cambridge CB3 0HA, UK*
[3]*INAF – Istituto di Radioastronomia, Via Gobetti 101, I-40129 Bologna, Italy*
[4]*Centre for Astrophysics Research, University of Hertfordshire, College Lane, Hatfield AL10 9AB, UK*

Accepted 2022 July 1. Received 2022 June 28; in original form 2022 April 22

ABSTRACT

Understanding whether and when the accretion disc extends down to the innermost stable circular orbit is important since it is the fundamental assumption behind measuring black hole spin. Here, we examine the 2013 and 2018 *NuSTAR* and *Swift* data (0.5–50 keV) of the narrow-line Seyfert 1 galaxy, WKK 4438. The X-ray emission can be fitted well with models depicting a corona and blurred reflection originating from a disc around a low-spin ($a_* \approx 0$) black hole. However, such models result in unconventional values for some of the parameters (e.g. inverted emissivity profile and high coronal height). Alternatively, equally good fits can be achieved if the disc is truncated at $\sim 10\,r_g$ and the black hole is spinning at the Thorne limit ($a_* = 0.998$). In these cases, the model parameters are consistent with the interpretation that the corona is centrally located close to the black hole and illuminating the disc at a larger distance.

Key words: galaxies: active – galaxies: nuclei – galaxies: individual: WKK 4438 – X-ray: galaxies.

1 INTRODUCTION

Disc truncation is a common explanation for describing the low-luminosity phases of the hard state of stellar mass black hole binaries and the behaviour of low-luminosity active galactic nuclei (LLAGNs). In the case of LLAGNs, the standard disc is truncated at large radii and the inner region is described by a hot, slow accretion flow that is radiatively inefficient (e.g. Narayan & Yi 1994; Lasota et al. 1996; Gammie, Narayan & Blandford 1999; Ptak et al. 2004).

Disc truncation is less common and perhaps unexpected in objects that are radiating efficiently and where the flow can be described by an optically thick, geometrically thin α-disc (Shakura & Sunyaev 1973). Indeed, these are exactly the objects where the black hole spin parameter ($a_* = a/M = Jc/GM^2$) can be measured well using thermal continuum fitting and Fe Kα modelling (e.g. Brenneman & Reynolds 2006; Shafee et al. 2006; see Reynolds 2021 for a recent review). Both of these techniques rely on the assumption that the disc edge extends down to the innermost stable circular orbit (ISCO). Therefore, it is important to examine whether there are radiatively efficient AGNs where this assumption does not hold.

WKK 4438 (IGR J14552−5133, LEDA 3076910; $z = 0.016$; Masetti et al. 2006) is located towards the Galactic Centre and viewed through a Galactic column density of 4.34×10^{21} cm^{-2} (Willingale et al. 2013). The AGN is relatively bright and it was detected in the *Swift*-BAT survey (Oh et al. 2018). Based on its optical emission line properties (Masetti et al. 2006), it is formally defined as a narrow-line Seyfert 1 (NLS1); however, its X-ray properties are less extreme than typical NLS1s (e.g. Grupe 2004; Grupe et al. 2004; Waddell & Gallo 2020, 2022). The most detailed X-ray study of the object was based on the 2012 *Suzaku* and short 2013 *NuSTAR* observations by Jiang et al. (2018b). They found tentative evidence of an ultrafast outflow and indication for a large inner disc radius.

In this work, the 0.5–50 keV emission of WKK 4438 is examined using new *NuSTAR* and *Swift* data from 2018 in conjunction with the previous 2013 data. The data are described in the following section. The variability and spectral analysis are presented in Sections 3 and 4, respectively. Discussion and concluding remarks are provided in Section 5.

2 OBSERVATION AND DATA REDUCTION

WKK 4438 was observed with *NuSTAR* (Harrison et al. 2013) on two occasions: the first time on 2013 September 19 for a duration of ~ 40 ks and the second time starting on 2018 September 21 for a duration of ~ 200 ks (PI: J. Jiang). At both epochs, a snapshot observation was obtained with the X-ray Telescope (XRT; Burrows et al. 2005) on the *Neil Gehrels Swift Observatory* (Gehrels et al. 2004). A summary of the observations used in this work is provided in Table 1.

The *Swift* XRT spectra (0.3–10 keV) were generated using the XRT data product generator[1] (Evans et al. 2009) for the specific dates of the *NuSTAR* observations. The XRT was operated in photon counting mode. The *NuSTAR* data were processed in the standard manner[2] with the *NuSTAR* Data Analysis Software NUSTARDAS v2.0.0 and calibration files from the *NuSTAR* CALDB v20200811. Both focal plane modules (FPMA and FPMB) operated normally and generated data. Unfiltered event files were cleaned with NUPIPELINE with the

★ E-mail: lgallo@ap.smu.ca

[1]https://www.swift.ac.uk/user_objects
[2]https://heasarc.gsfc.nasa.gov/docs/nustar/analysis/nustar_swguide.pdf

Table 1. The observation log of the X-ray spectral data utilized in the analysis of WKK 4438. The observatories and instruments used are listed in column (1). The ID corresponding to the observation is given in column (2). The start date and total good-time exposure follow in columns (3) and (4). The total source counts (background corrected) are given in column (5) for the combined FBMA + FBMB in 2018 (4–50 keV) and 2013 (4–30 keV), and for the XRT (0.5–4 keV).

(1) Observatory (instruments)	(2) Observation ID	(3) Start date (year.mm.dd)	(4) Exposure (ks)	(5) Source counts
NuSTAR	60061259002	2013.09.19	21.9	5985
	60401022002	2018.09.21	100.9	33 515
(FPMA + FBMB)				
Swift	00080140001	2013.09.20	7.1	639
(XRT)	00088730001	2018.09.22	2.1	214

default settings on mode 1 data only. Light curves and spectra were extracted from the data using NUPRODUCTS, which also creates the spectral response matrices. *NuSTAR* source data were extracted from a circular region with a radius of 75 arcsec centred on the source. The background was selected from a nearby circular region with a radius of 110 arcsec.

The 2012 *Suzaku* light curve (0.5–10 keV) of WKK 4438 from the combined front-illuminated CCDs is presented in Fig. 1. The data come from products generated by Waddell & Gallo (2020) and are presented here for comparison. Detailed examination of the *Suzaku* spectra was carried out by Jiang et al. (2018b).

3 RAPID FLUX VARIATIONS

The 2013 and 2018 *NuSTAR* (4–30 keV) light curves as well as the 2012 *Suzaku* (0.5–10 keV) light curves from the combined front-illuminated CCDs are shown in Fig. 1. Substantial variations, up to ±50 per cent, are present in both energy ranges and on all time-scales probed with the data (i.e. ks to days). However, spectral variations as demonstrated from hardness ratios (Fig. 1) and fractional variability analysis are modest. The *NuSTAR* spectra between 2013 and 2018 are quite similar. A difference spectrum between the two epochs can be fitted between 4 and 30 keV with a single power law ($\Gamma \sim 2.1$) indicating the differences are dominated by flux changes (Fig. 2).

For a black hole mass of $2 \times 10^6\,M_\odot$ in WKK 4438 (Malizia et al. 2008), $10\,r_g$ corresponds to a light-crossing time of ~ 100 s and a dynamical time-scale of ~ 2 ks. The high-amplitude and rapid variations on a kilosecond time-scale in WKK 4438 indicate that the X-rays are originating from a compact region. The insignificant spectral variations would suggest that only one component might dominate the X-ray band or that multiple components vary in such a way as to not change the overall shape of the spectrum.

4 SPECTRAL ANALYSIS

All spectra are grouped using optimal binning (Kaastra & Bleeker 2016). To utilize Cash statistics (Cash 1979, see below) effectively, the background spectra are fitted separately with a phenomenological model comprising a blackbody, power law, and Gaussian profiles for instrumental emission lines (Fig. 2). The data are analysed in regions where the source is dominant over the background and the calibration is well understood. For the 2013 and 2018 *NuSTAR* data, this corresponds to 4–30 and 4–50 keV, respectively. To constrain the low-energy emission, *Swift* XRT data obtained simultaneously with each *NuSTAR* observation are used between 0.5 and 4 keV. Given the low count rate, many XRT bins above 4 keV have zero counts. The parameters are linked between data sets at each epoch except for a calibration constant between the two FPM detectors and another constant between *NuSTAR* and *Swift*. Both calibration constants are in agreement with the expected values. Both epochs are fitted simultaneously.

Spectral fitting was performed using XSPEC V12.11.1 and the fit quality was evaluated by minimizing the modified C-statistic (based on the Cash statistic, Cash 1979; Humphrey, Liu & Buote 2009) in XSPEC. Parameter uncertainties for the best-fitting models were determined using a Markov chain Monte Carlo (MCMC). Using the XSPEC implementation of the Goodman & Weare (2010) algorithm, the MCMC was run with 100 walkers for 2.2×10^5 steps and

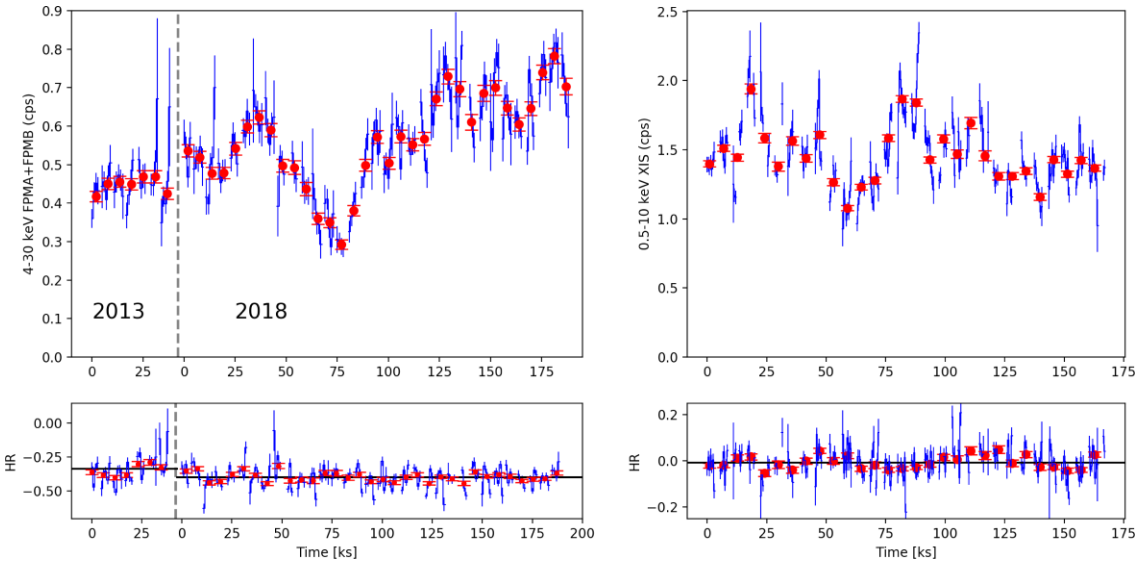

Figure 1. *NuSTAR* (left-hand panels) and *Suzaku* (right-hand panels) light curves (upper panels) and hardness ratio curves where HR = $(H - S)/(H + S)$ (lower panels). The blue points are 1000 s bins and the red points are orbital bins (5760 s). For the *NuSTAR* hardness ratios, H = 10–30 keV and S = 4–10 keV. For *Suzaku*, H = 2–10 keV and S = 0.5–2 keV.

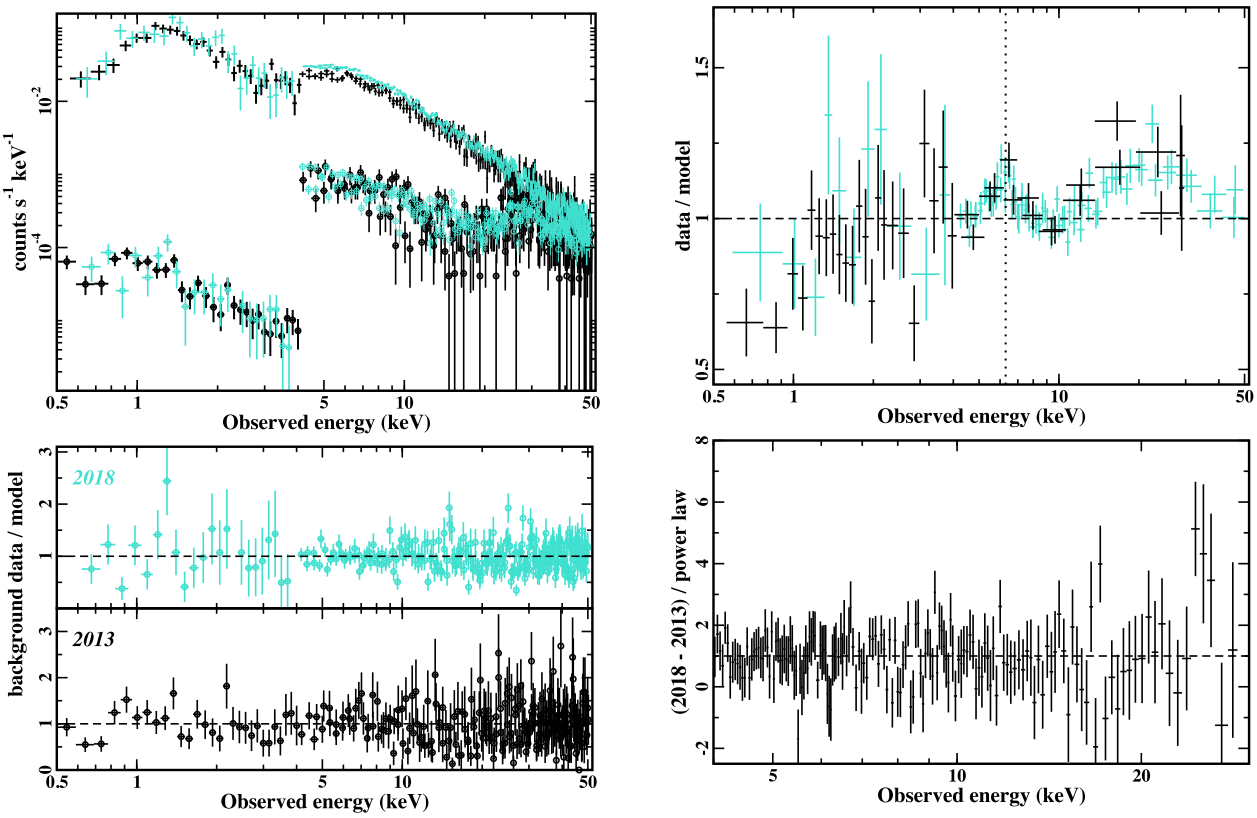

Figure 2. The spectral data from the 2013 (black) and 2018 (turquoise) observations of WKK 4438. The *NuSTAR* data are above 4 keV and the *Swift* XRT data are below 4 keV. The corresponding background spectra are shown with circular data points. Upper left-hand panel: the spectral data from each epoch and telescope compared to respective background levels. Data from FPMA and FPMB are plotted, but shown as the same colour to ease comparison between epochs. Lower left-hand panel: the data-to-model ratio for the background spectra of each instrument. The background model is phenomenological consisting of a blackbody, power law, and Gaussian profiles for instrumental emission lines. Upper right-hand panel: the data-to-model ratio of an absorbed power law fitted to the spectra in the ranges 4–5, 7.5–10, and 40–50 keV, and extrapolated over the entire band. Excess emission is evident between 10 and 40 keV, and in the Fe Kα band. The vertical dotted line marks 6.4 keV in the source frame. The spectrum below ~ 1.5 keV is lower than predicted from the extrapolated power law. Lower right-hand panel: the difference spectrum between the 2018 and 2013 *NuSTAR* data can be fitted with a single power law ($\Gamma \sim 2.1$). The data from each instrument are combined at each epoch.

burning the first 20 000 steps. The reported values are the mean of the likelihood function and the uncertainties correspond to the 90 per cent confidence interval.

For the final models, the Deviance Information Criterion (DIC; Spiegelhalter et al. 2002) is used to compare different models and quantify a goodness of fit (the C-statistic is used for preliminary models in limited energy ranges). Using the MCMC posterior distribution, the DIC adds a penalty for the effective number of free parameters (i.e. half the variance of the distribution; Gelman et al. 2003) to the posterior mean fit statistic. A smaller DIC value favours one model over another. A difference in DIC (ΔDIC) between 0 and 2 indicates a marginal preference for a model, whereas $\Delta\mathrm{DIC} > 6$ reflects a strong preference (Kass & Raftery 1995).

All parameters are reported in the rest frame of the source unless specified otherwise, but figures remain in the observed frame. A value of the total Galactic column density, considering atomic and molecular hydrogen, towards WKK 4438 of 4.34×10^{21} cm^{-2} (Willingale et al. 2013) and appropriate abundances (Wilms, Allen & McCray 2000) are adopted in all spectral fits. All final models will require addition neutral absorption on the level of $\sim 10^{21}$ cm^{-2} that is local to WKK 4438.

Fitting a power law to the spectra in the ranges 4–5, 7.5–10, and 40–50 keV, and extrapolated over the entire band reveals an excess of emission in the Fe Kα band (6–7 keV) and within 10–40 keV (Fig. 2). However, unlike most Seyfert 1 galaxies, there is no soft excess evident below ~ 2 keV, but rather a dearth. This is likely from additional absorption local to WKK 4438.

A Gaussian profile with free energy and width (σ) is substantially better than a narrow ($\sigma = 1$ eV) profile with the energy fixed at $E = 6.4$ keV ($\Delta C = -27$ for two additional parameters). In this case, the centroid energy is $6.20^{+0.20}_{-0.36}$ keV and the width is $\sigma = 0.67^{+0.41}_{-0.26}$ keV. Assuming that the width of the line is attributed to velocity broadening from material in a Keplerian orbit, the emission would originate at a distance of $66^{+39}_{-51}\, r_{\rm g}$ from the black hole.

The absorption features reported by Jiang et al. (2018b) and attributed to an ultrafast outflow with argon and iron overabundances are less conspicuous in the 2018 data (Fig. 2). Applying the same absorption grid used in Jiang et al. (2018b) with all wind parameters allowed to vary does not improve the fit significantly. The feature previously attributed to iron is negligible in the new data and now results in sub-solar iron abundances. Alternatively, fixing all wind parameters to the values found in Jiang et al. (2018b) except for the column density finds a value of $\lesssim 7 \times 10^{22}$ cm^{-2}. This is comparable to $\sim 12 \times 10^{22}$ cm^{-2} found by Jiang et al. (2018b). Variability of the ultrafast outflow is possible and could explain the differences in appearance with the earlier *Suzaku* and *NuSTAR* observations (Jiang

et al. 2018b). However, the features are not considered further here, and it is noted that the continuum measurements found here are comparable to the work of Jiang et al. (2018b), which included a wind component in their model. Therefore, accounting for those features does not significantly impact the continuum results.

Introducing a XILLVERCP (García & Kallman 2010) component to model distant, neutral reflection along with additional host-galaxy absorption provided a reasonable fit (C/d.o.f. = 1012.5/898, where d.o.f. is the degrees of freedom, and DIC = 1022.6). This will serve as the baseline model to compare subsequent fits. The apparent absence of a soft excess, which could be from an excess of absorption and/or from a weak soft component, is unusual for a Seyfert 1. To examine for a soft excess, multicomponent continuum models are attempted. Following Petrucci et al. (2018), the primary continuum is modelled with two NTHCOMP (Zdziarski, Johnson & Magdziarz 1996; Życki, Done & Smith 1999) components to replicate two coronae (e.g. Magdziarz et al. 1998; Czerny et al. 2003; Ballantyne 2020). The warm and hot coronae are each allowed to have their own electron temperatures ($kT_e^{\rm wc}$ and $kT_e^{\rm hc}$, respectively), but share a common blackbody disc temperature ($kT_{\rm bb} = 0.05$ keV). The additional host-galaxy column density and a distant reflector remain in the model. During initial fits, the temperature of the warm corona that accounts for the putative soft excess was not constrained. Consequently, this parameter was fixed to a typical value of $kT_e^{\rm wc} = 1$ keV (Petrucci et al. 2018). The double Comptonization model attaches a soft-excess component in the intrinsic X-ray spectrum of WKK 4438, which may be more plausible, but the fit is statistically less likely than the baseline single power law and distant, neutral reflector (ΔDIC = +5.7).

Alternatively, a natural explanation for the excess emission at ~ 20 keV and in the Fe Kα band, which is broad and redwards of the neutral line, is relativistically blurred reflection from the inner disc (e.g. Ross & Fabian 2005). This model also accounts for fluorescent emission from lower atomic number elements that contribute to forming a so-called soft excess. The distant reflector is replaced with blurred reflection using the RELXILL suite of models (Dauser et al. 2010; García & Kallman 2010). Initially, several flavours of RELXILL were tested with various combinations of free parameters. Allowing for variable densities or coronal electron temperatures never improved the fits, so these parameters are fixed to their canonical values of $N = 10^{15}$ cm^{-3} and $kT_e = 100$ keV, respectively. In addition, the black hole spin, disc inclination (i), and iron abundance ($A_{\rm Fe}$) are linked between epochs.

Two reasonable blurred reflection fits were achieved using RELXILLD (C/d.o.f. = 993.1/890 and DIC = 1011.1) and RELXILLLP (C/d.o.f. = 1004.1/891 and DIC = 1025.8), separately. With the former, the emissivity profile for the accretion disc is described by a broken power law, where the profile goes as $r^{-q_{\rm in}}$ from the inner disc edge ($R_{\rm in}$) to the break radius $R_{\rm b}$, where it then changes to $r^{-q_{\rm out}}$. Beyond the break radius of $R_{\rm b}$, the outer emissivity index is set to the classical value of $q_{\rm out} = 3$. Such a model depicting differing illumination patterns could be indicative of different coronal geometries (e.g. Wilkins & Fabian 2012).

With RELXILLLP, the corona is assumed to be a point source that is located on the spin axis at some height above the disc (i.e. a lamp post). Here, the height of the corona point source is the model parameter and the illumination pattern on the disc (i.e. the emissivity profile) is determined from that. There have been significant advances in spectral modelling (e.g. Dauser et al. 2013; Wilkins & Gallo 2015b; Gonzalez, Wilkins & Gallo 2017; Jiang et al. 2022) and reverberation mapping (e.g. Caballero-García et al. 2018, 2020; Alston et al. 2020) that have enabled good measurements of the coronal height in other AGN. Both spectral and timing methods provide comparable estimates when applied to the same source.

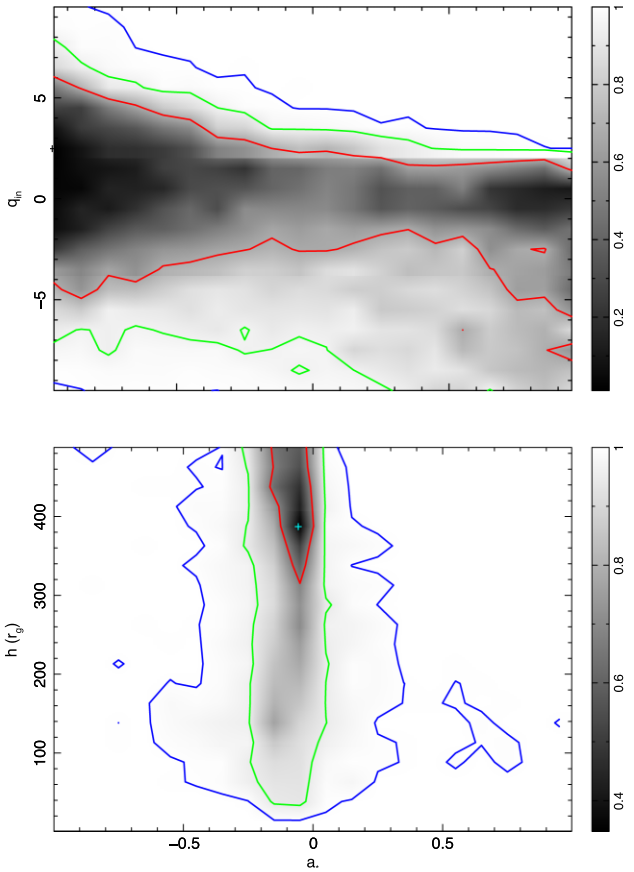

Figure 3. The integrated probability density contours assuming the inner disc radius extends down to the ISCO render the following behaviour between some parameters. Upper panel: the inner emissivity index and black hole spin are both consistent with low values, though neither is well constrained. Lower panel: in the lamp-post scenario, the spin is tightly constrained near zero, and large values for the height of the point source corona are preferred. The contour levels depicted are 0.68, 0.95, and 0.997.

In both reflection models presented, the fundamental assumption is that the inner disc edge ($R_{\rm in}$) extends down to the ISCO, which is driven by the angular momentum of the black hole defined by the spin parameter (a_*).

While both models provide reasonable fits to the spectra, the fits do have some unusual characteristics. For the RELXILLD interpretation, though both the inner disc emissivity profile and black hole spin are poorly constrained, the best-fitting values are both small and negative (Fig. 3). This would indicate that the disc brightens with increasing distance and the black hole spin is retrograde. For the lamp-post model, the best-fitting height parameter suggests that the point source corona is at $h > 128\,r_{\rm g}$, corresponding to a light-traveltime of over 30 min for a 2×10^6 M$_\odot$ black hole (Malizia et al. 2008). The black hole spin is well constrained in this model to be retrograde and near zero ($a_* = -0.09^{+0.03}_{-0.17}$).

The combination of parameters measured with these models is atypical, notably the low spin parameter. Nearly all of the three dozen black hole spin parameters measured in active galaxies are consistent with high spins ($a_* > 0.9$; e.g. Reynolds 2021). There are several reasons for this including cosmological (e.g. Berti & Volonteri 2008), selection effects (e.g. Reynolds 2021) and the

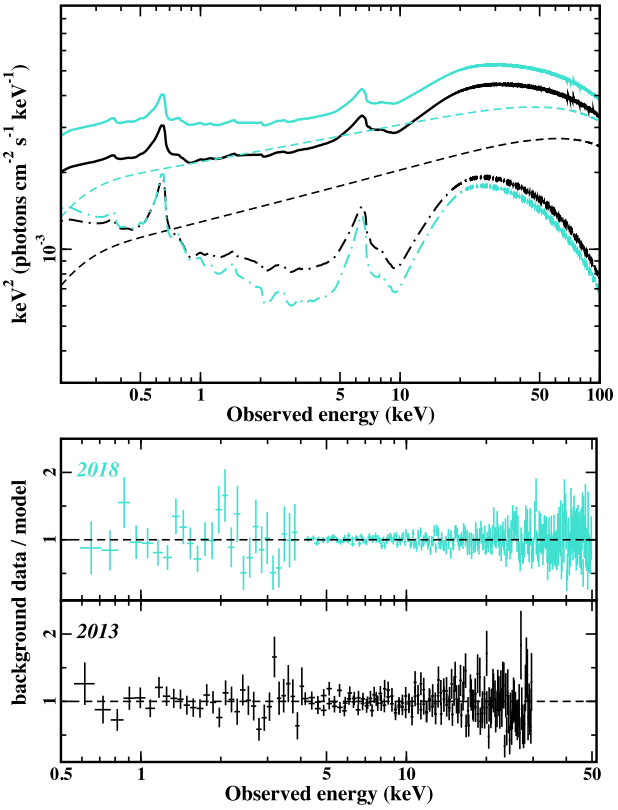

Figure 4. Upper panel: the components of the best-fitting blurred reflection model (Table 2) with the Galactic and host column density removed. The solid curves are the total models (black for 2013 and turquoise for 2018). The power law and blurred reflector are shown as dashed curves and dot–dashed curves, respectively. Lower panels: the data-to-model residuals remaining in the spectrum of each epoch.

general difficulty with measuring low spins robustly from limited bandpass data (e.g. Bonson & Gallo 2016). For those reasons, the same two blurred reflection models were applied to WKK 4438, but without the fundamental assumption that the inner disc edge reaches the ISCO. Rather, the black hole spin parameter is fixed to the maximum value ($a_* = 0.998$; Thorne 1974) and the inner accretion disc radius is permitted to vary freely. Compared to the models with variable spin, the model with fixed maximum spin and free inner disc radius was comparably good with RELXILLD (ΔDIC $= +2.8$) and significantly better in the RELXILLLP case (ΔDIC $= -10.0$).

For the RELXILLD model, in addition to $R_{\rm in}$, the inner emissivity profile $q_{\rm in}$ was also allowed to vary. This did not enhance the fit or constrain the parameter, basically mimicking the behaviour in Fig. 3. For simplicity, in the final fit, we assumed $q = 3$ across the entire disc commensurate with a Newtonian system. This generated a good fit (C/d.o.f. $= 995.5/892$ and DIC $= 1013.9$), and while statically it is slightly less preferred than the scenario with $R_{\rm in} = r_{\rm ISCO}$ (ΔDIC $= +2.8$), the model parameters seem more plausible (Fig. 4 and Table 2) in our view since low/retrograde spins and inverted emissivity profiles are not required. In this scenario, the inner disc radius is relatively well constrained to $9.9^{+20.1}_{-5.4}\,r_{\rm g}$; thus, having the disc extending down to the ISCO of a Kerr black hole ($r_{\rm ISCO} = 1.25\,r_{\rm g}$) is unlikely (Fig. 5).

The RELXILLLP model with a Kerr black hole and free $R_{\rm in}$ also produces a good fit (C/d.o.f. $= 997.8/891$ and DIC $= 1015.8$) that is comparable to the RELXILLD model with free $R_{\rm in}$ (ΔDIC $= +1.9$). Here, the inner radius is poorly constrained, but the best fit is with

Table 2. The blurred reflection model fitted to the 2018 and 2013 WKK 4438 spectra. The model components and model parameters are listed in columns 1 and 2, respectively. Columns 3 and 4 list the parameter values during the 2018 and 2013 observations, respectively. The photon index of the reflection components is linked to the photon index measured by NTHCOMP. The reflection fraction ($\mathcal{R}$) is calculated as the ratio of the reflected flux over the power-law flux in the 0.1–100 keV band and is based on the best-fitting parameters. Setting $\mathcal{R}$ as a fit parameter in the RELXILLD model generates similar values. The cutoff temperature in RELXILLD is fixed at $E_c = 300$ keV. Values that are linked between epochs appear only in column 3.

(1) Model component	(2) Model parameter	(3) 2018	(4) 2013
Neutral absorption (ZTBABS)	$N_{\rm H}$ ($\times 10^{21}$ cm^{-2})	$1.78^{+0.86}_{-0.75}$	
Power law (NTHCOMP)	Γ	$1.87^{+0.13}_{-0.08}$	$1.80^{+0.10}_{-0.12}$
	kT_e/ keV	100^f	
	$kT_{\rm bb}$/ keV	0.05^f	
	norm ($\times 10^{-3}$)	$2.20^{+0.98}_{-0.59}$	$1.29^{+0.73}_{-0.92}$
Blurred reflection (RELXILLD)	q	3^f	
	$R_{\rm in}/r_{\rm g}$	$9.9^{+20.1}_{-5.4}$	
	$R_{\rm out}/r_{\rm g}$	400^f	
	a_*	0.998^f	
	i/°	24^{+14}_{-15}	
	Γ	1.87	1.80
	log(ξ/ erg cm s^{-1})	$2.98^{+0.32}_{-0.95}$	$3.11^{+0.48}_{-0.47}$
	$A_{\rm Fe}/A_\odot$	$1.00^{+1.94}_{-0.22}$	
	log(N/ cm^{-3})	15^f	
	norm ($\times 10^{-5}$)	$1.09^{+0.56}_{-0.26}$	$1.07^{+0.53}_{-0.40}$
	$\mathcal{R}$	$0.46^{+0.32}_{-0.17}$	$0.75^{+0.57}_{-0.60}$
Calibration constant	*NuSTAR*	0.99 ± 0.02	0.94 ± 0.04
	Swift	0.92 ± 0.12	0.97 ± 0.10
Fit quality	C/d.o.f.	995.5/892	
	DIC	1013.9	

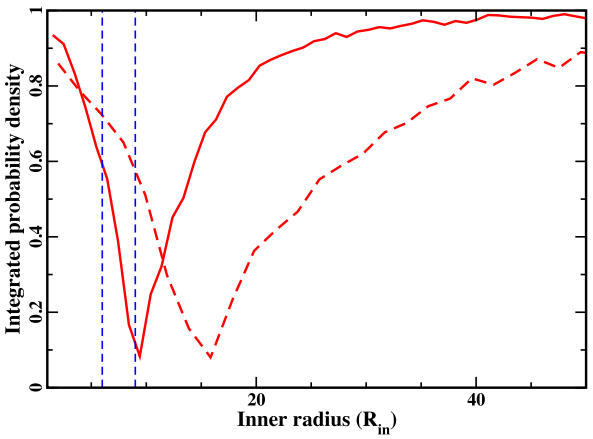

Figure 5. Assuming a Kerr black hole with the inner disc radius truncated beyond $r_{\rm ISCO}$ provides a better statistical fit with more plausible parameters. The constraints on the inner disc radius for the RELXILLD (solid red curve) and RELXILLLP (dashed red curve) are shown. The parameter is better constrained with RELXILLD and both models favour an inner disc that does not extend to the ISCO. The blue vertical lines mark the radii expected in a Schwarzschild black hole ($6\,r_{\rm g}$) and one with maximum retrograde spin ($9\,r_{\rm g}$).

$R_{\rm in} \sim 15\,r_{\rm g}$, similar to the RELXILLD case. The height of the corona is well constrained to be $7.5^{+5.1}_{-2.5}\,r_{\rm g}$ unlike how poorly constrained the height was in the RELXILLLP model with variable spin (Fig. 3). It is notable that leaving $R_{\rm in}$ free to vary or tying it to the ISCO and changing a_* actually results in comparable values for the location of the inner edge.

5 DISCUSSION AND CONCLUSION

WKK 4438 exhibits rapid flux variability on short time-scales, but spectral variations appear minimal. Two *NuSTAR* observations from 2013 and 2018 are examined here, and both are relatively consistent, except for a modest change in brightness. The photon indices measured here are also comparable to the earlier 2006 and 2007 *Swift* XRT data (Malizia et al. 2008).

The 0.5–50 keV spectra at both epochs can be described well with a blurred reflection scenario where some of the primary emission from the corona illuminates the inner accretion disc and is backscattered in the direction of the observer (e.g. Ross & Fabian 2005). Applying the reflection models with the standard assumption that the inner edge of the accretion disc extends down to the ISCO results in an unexpected combination of parameter values and requires an unconventional interpretation.

For example, when adopting a RELXILL scenario, the black hole spin parameter and inner emissivity index are poorly constrained, but positive spin values ($a_* > 0$) in combination with steep emissivity profiles ($q_{\rm in} > 5$), as might be expected, are significantly ruled out. Instead, high spin values are better paired with inverted emissivity profiles, and conversely, low (retrograde) spins with higher $q_{\rm in}$ (Fig. 3). Both of these conditions imply that the inner disc emission close to the black hole is weak – either the inner disc is located at large distances because the black hole spins slowly or the disc is brighter at larger distances. Similarly, the lamp-post scenarios (RELXILLLP) find a large height, which is poorly constrained, for the point source corona (Fig. 3), but tightly constrain the spin parameter to $a_* \approx 0$.

However, models assuming that WKK 4438 possesses a maximum spinning black hole with its inner disc truncated at larger distances generate similar (or better) fits and more sensible parameters. In these cases, the inner disc does not extend down to the ISCO, but is truncated at $5–20\,r_{\rm g}$. The flatter emissivity profiles ($q = 3$) and low reflection fractions ($\mathcal{R} < 1$) that are found in these models follow from the interpretation that the accretion disc inner edge might not extend into the immediate vicinity of the black hole where the general relativistic effects that produce large $\mathcal{R}$ and q are at work. With these maximum-spin models, the measured corona height in WKK 4438 is also better constrained and comparable to the heights measured in other systems (e.g. Gallo et al. 2015; Caballero-García et al. 2018, 2020; Alston et al. 2020; Gonzalez et al . 2020).

One could also have a situation where the lamp post is at some horizontal distance and orbits the rotation axis. This might enhance the disc brightness at larger distances, but the inner edge should still be detectable (e.g. Wilkins & Fabian 2012; Gonzalez et al. 2017). This scenario would not change the measured inner radius seen here, which appears independent of the black hole spin.

During the fainter stages of the hard state of black hole binaries, truncated discs are common (e.g. Esin, McClintock & Narayan 1997). For supermassive black holes, such discs are typically associated with LLAGNs where the standard disc (Shakura & Sunyaev 1973) is truncated at $> 100\,r_{\rm g}$ and the inner flow is replaced with a hot, radiative inefficient flow (e.g. Narayan & Yi 1994; Lasota et al. 1996) that is extremely sub-Eddington ($L/L_{\rm Edd} < 10^{-3}$).

WKK 4438 does not exhibit the characteristics of an LLAGN. Following Brightman et al. (2013), based on the measured photon indices in 2013 and 2018, $L/L_{\rm Edd} = 0.03–0.06$. Even though the luminosity ratio is not particularly high, the value is consistent with a standard accretion disc. Its ultraviolet (UV) bump is probably present given the estimated UV-to-X-ray spectral slope of $\alpha_{\rm ox} \sim -1.40$ (Panessa et al. 2011) and WKK 4438 does not appear to be radio-loud or exhibit synchrotron emission related to jets. It is not detected in the TIFR GMRT Sky Survey (Intema et al. 2017) and has a 3σ upper limit of <10 mJy at 150 MHz, nor is it detected at 72–231 MHz in the GLEAM survey (Wayth et al. 2015). WKK 4438 is also highly variable in the X-rays, contrary to most LLAGNs (e.g. Ptak et al. 1998; Younes et al. 2019), and it possesses a broad Fe Kα line and Compton hump, which are not normally seen in LLAGNs (e.g. Dewangan et al. 2004; Ptak et al. 2004; Reynolds et al. 2009; Lobban et al. 2010; Younes et al. 2019).

Noteworthy, WKK 4438 is categorized as an NLS1 by Masetti et al. (2006). Only an upper limit could be measured for the Fe II emission, but in conjunction with the other optical properties it does meet the criteria. This is of interest because the class includes some extreme objects that are well known for emitting X-rays from a compact region close to a Kerr black hole (e.g. Fabian et al. 2009; Jiang et al. 2018a; Wilkins et al. 2022; see Gallo 2018 for review). This appears contradictory to the behaviour of WKK 4438, whose inner disc is at approximately $10\,r_{\rm g}$. It is worth noting that WKK 4438 was anomalous compared to other NLS1s observed with *Suzaku* (Waddell & Gallo 2020, 2022). Compared to other NLS1s in the *Suzaku* sample, WKK 4438 possesses relatively weak reflection features and soft excess, and a low Eddington luminosity ratio, which are more consistent with typical Seyfert 1 galaxies. The contradiction may speak to the need for a better definition of the NLS1 phenomenon.

If the corona is covering a large fraction of the inner disc, the reflection spectrum could be highly Comptonized (e.g. Petrucci et al. 2001; Wilkins & Gallo 2015a) making the inner disc appear truncated. This does not seem applicable in WKK 4438 as the continuum spectrum is rather typical in shape. A cursory application of such a model (COMPTONISE; Wilkins & Gallo 2015a) to the data shows that the covering fraction is rather low (∼5 per cent) and the reflection parameters are not dissimilar to the previous fits in this work.

WKK 4438 is relatively underexamined. The *NuSTAR* data presented here are the highest quality to date, but do not extend below ~ 4 keV. The host galaxy exists in an optically crowded field (see fig. 2 in the online material of Masetti et al. 2006) and has not been investigated significantly. Perhaps a recent merger could have disrupted the disc and it is now refilling. The line of sight is also moderately absorbed by the Galaxy and the host ($\sim 10^{21}$ cm^{-2}) making inspection of the soft band more challenging. Understanding whether and when the disc does extend to the ISCO is important since it is the fundamental assumption behind measuring the black hole spin (e.g. Brenneman & Reynolds 2006; Shafee et al. 2006; see Reynolds 2021 for a recent review). It is necessary to determine how often this assumption may be invalid.

Our analysis suggests that WKK 4438 might have a low or retrograde spinning black hole, but the more likely possibility is that the disc is truncated and the black hole spins rapidly. Future observations with *XMM–Newton* and *NuSTAR* will constrain the soft X-ray emission and search for frequency-dependent lags. Studies of

the host galaxy will confirm the behaviour and origin of the truncated disc in WKK 4438.

ACKNOWLEDGEMENTS

The authors thank the referee for comments that improved the manuscript. This research has made use of data obtained with *NuSTAR*, a project led by Caltech, funded by NASA and managed by NASA/JPL. LCG acknowledges financial support from the Natural Sciences and Engineering Research Council of Canada (NSERC) and from the Canadian Space Agency (CSA). JJ acknowledges support from the Leverhulme Trust, the Isaac Newton Trust, and St Edmund's College, University of Cambridge.

DATA AVAILABILITY

The data used in this study are available in the *NuSTAR* and *Swift* public archives.

REFERENCES

Alston W. N. et al., 2020, Nat. Astron., 4, 597
Ballantyne D. R., 2020, MNRAS, 491, 3553
Berti E., Volonteri M., 2008, ApJ, 684, 822
Bonson K., Gallo L. C., 2016, MNRAS, 458, 1927
Brenneman L. W., Reynolds C. S., 2006, ApJ, 652, 1028
Brightman M. et al., 2013, MNRAS, 433, 2485
Burrows D. N. et al., 2005, Space Sci. Rev., 120, 165
Caballero-García M. D., Papadakis I. E., Dovčiak M., Bursa M., Epitropakis A., Karas V., Svoboda J., 2018, MNRAS, 480, 2650
Caballero-García M. D., Papadakis I. E., Dovčiak M., Bursa M., Svoboda J., Karas V., 2020, MNRAS, 498, 3184
Cash W., 1979, ApJ, 228, 939
Czerny B., Nikołajuk M., Różańska A., Dumont A. M., Loska Z., Zycki P. T., 2003, A&A, 412, 317
Dauser T., Wilms J., Reynolds C. S., Brenneman L. W., 2010, MNRAS, 409, 1534
Dauser T., Garcia J., Wilms J., Böck M., Brenneman L. W., Falanga M., Fukumura K., Reynolds C. S., 2013, MNRAS, 430, 1694
Dewangan G. C., Griffiths R. E., Di Matteo T., Schurch N. J., 2004, ApJ, 607, 788
Esin A. A., McClintock J. E., Narayan R., 1997, ApJ, 489, 865
Evans P. A. et al., 2009, MNRAS, 397, 1177
Fabian A. C. et al., 2009, Nature, 459, 540
Gallo L., 2018, in Anton S., ed., Revisiting Narrow-Line Seyfert 1 Galaxies and Their Place in the Universe. Proceedings of Science, Padova, p. 34
Gallo L. C. et al., 2015, MNRAS, 446, 633
Gammie C. F., Narayan R., Blandford R., 1999, ApJ, 516, 177
García J., Kallman T. R., 2010, ApJ, 718, 695
Gehrels N. et al., 2004, ApJ, 611, 1005
Gelman A., Carlin J., Stern H., Rubin D., 2003, Texts in Statistical Science, Bayesian Data Analysis. 2ndedn. Taylor & Francis, London
Gonzalez A. G., Wilkins D. R., Gallo L. C., 2017, MNRAS, 472, 1932
Gonzalez A. G., Gallo L. C., Kosec P., Fabian A. C., Alston W. N., Berton M., Wilkins D. R., 2020, MNRAS, 496, 3708
Goodman J., Weare J., 2010, Commun. Appl. Math. Comput. Sci., 5, 65
Grupe D., 2004, AJ, 127, 1799
Grupe D., Wills B. J., Leighly K. M., Meusinger H., 2004, AJ, 127, 156
Harrison F. A. et al., 2013, ApJ, 770, 103
Humphrey P. J., Liu W., Buote D. A., 2009, ApJ, 693, 822
Intema H. T., Jagannathan P., Mooley K. P., Frail D. A., 2017, A&A, 598, A78
Jiang J. et al., 2018a, MNRAS, 477, 3711
Jiang J., Walton D. J., Parker M. L., Fabian A. C., 2018b, MNRAS, 481, 639
Jiang J., Dauser T., Fabian A. C., Alston W. N., Gallo L. C., Parker M. L., Reynolds C. S., 2022, MNRAS, 514, 1107
Kaastra J. S., Bleeker J. A. M., 2016, A&A, 587, A151
Kass R. E., Raftery A. E., 1995, J. Am. Stat. Assoc., 90, 773
Lasota J. P., Abramowicz M. A., Chen X., Krolik J., Narayan R., Yi I., 1996, ApJ, 462, 142
Lobban A. P., Reeves J. N., Porquet D., Braito V., Markowitz A., Miller L., Turner T. J., 2010, MNRAS, 408, 551
Magdziarz P., Blaes O. M., Zdziarski A. A., Johnson W. N., Smith D. A., 1998, MNRAS, 301, 179
Malizia A. et al., 2008, MNRAS, 389, 1360
Masetti N. et al., 2006, A&A, 459, 21
Narayan R., Yi I., 1994, ApJ, 428, L13
Oh K. et al., 2018, ApJS, 235, 4
Panessa F. et al., 2011, MNRAS, 417, 2426
Petrucci P. O., Merloni A., Fabian A., Haardt F., Gallo E., 2001, MNRAS, 328, 501
Petrucci P. O., Ursini F., De Rosa A., Bianchi S., Cappi M., Matt G., Dadina M., Malzac J., 2018, A&A, 611, A59
Ptak A., Yaqoob T., Mushotzky R., Serlemitsos P., Griffiths R., 1998, ApJ, 501, L37
Ptak A., Terashima Y., Ho L. C., Quataert E., 2004, ApJ, 606, 173
Reynolds C. S., 2021, ARA&A, 59, 117
Reynolds C. S., Nowak M. A., Markoff S., Tueller J., Wilms J., Young A. J., 2009, ApJ, 691, 1159
Ross R. R., Fabian A. C., 2005, MNRAS, 358, 211
Shafee R., McClintock J. E., Narayan R., Davis S. W., Li L.-X., Remillard R. A., 2006, ApJ, 636, L113
Shakura N. I., Sunyaev R. A., 1973, A&A, 500, 33
Spiegelhalter D. J., Best N. G., Carlin B. P., Van Der Linde A., 2002, J. R. Stat. Soc. B, 64, 583
Thorne K. S., 1974, ApJ, 191, 507
Waddell S. G. H., Gallo L. C., 2020, MNRAS, 498, 5207
Waddell S. G. H., Gallo L. C., 2022, MNRAS, 510, 4370
Wayth R. B. et al., 2015, PASA, 32, e025
Wilkins D. R., Fabian A. C., 2012, MNRAS, 424, 1284
Wilkins D. R., Gallo L. C., 2015a, MNRAS, 448, 703
Wilkins D. R., Gallo L. C., 2015b, MNRAS, 449, 129
Wilkins D. R., Gallo L. C., Costantini E., Brandt W. N., Blandford R. D., 2022, MNRAS, 512, 761
Willingale R., Starling R. L. C., Beardmore A. P., Tanvir N. R., O'Brien P. T., 2013, MNRAS, 431, 394
Wilms J., Allen A., McCray R., 2000, ApJ, 542, 914
Younes G., Ptak A., Ho L. C., Xie F.-G., Terasima Y., Yuan F., Huppenkothen D., Yukita M., 2019, ApJ, 870, 73
Zdziarski A. A., Johnson W. N., Magdziarz P., 1996, MNRAS, 283, 193
Życki P. T., Done C., Smith D. A., 1999, MNRAS, 309, 561

This paper has been typeset from a TEX/LATEX file prepared by the author.